CMS Physics Analysis Summary

Contact: cms-pag-conveners-top@cern.ch 2021/03/20

Measurement of the inclusive and differential $\mathrm{t\bar{t}} + \gamma$ cross section and EFT interpretation in the single lepton channel at $\sqrt{s} = 13$ TeV

The CMS Collaboration

Abstract

The production cross section of a top quark pair in association with a photon is measured in proton-proton collisions at the center-of-mass energy of 13 TeV. The data set of 137 fb^{-1} was recorded by the CMS experiment during the LHC Run II. The measurement is performed in events with a well isolated, highly energetic lepton (electron or muon), with at least three jets from the hadronization of quarks and one isolated photon. The photon may be emitted from initial state radiation, from the top quarks, as well as from decay products of the top quarks. The analysis makes use of simultaneous likelihood fits in several signal and control regions to distinguish the $\mathrm{t\bar{t}} + \gamma$ signal process from various backgrounds. The inclusive cross section for a photon with transverse momentum of $p_T \geq 20$ GeV is measured as 800 ± 46 (syst) ± 7 (stat) fb, in good agreement with the prediction from the standard model. The measurement is also carried out differentially in several kinematic observables and interpreted in the framework of the standard model effective field theory.

1 Introduction

The large amount of proton-proton (pp) collision data at a center-of-mass energy of 13 TeV at the CERN LHC allows for precision measurements of standard model (SM) processes with very small production rates. Precision measurements of top quark production provide a testing ground for the SM predictions and for phenomena beyond the SM (BSM). Confronting inclusive and differential cross section measurements of top quark pair production in association with a high-energy photon allows to constrain the tγ electroweak coupling [1].

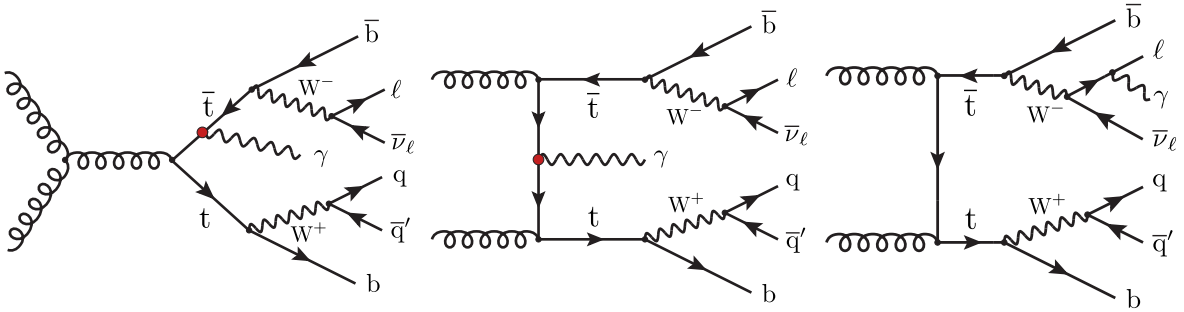

Figure 1: Representative LO Feynman diagrams for the t$\bar{\text{t}}\gamma$ signal process in the single lepton channel where the high energetic photon originates from the top quark (left, middle), or is emitted from a lepton (right). The tγ interaction is indicated by a circle.

The CDF Collaboration has measured the t$\bar{\text{t}}\gamma$ production cross section using p$\bar{\text{p}}$ collisions at $\sqrt{s} = 1.96$ TeV [2], while at the LHC the measurement has been performed in pp collisions at $\sqrt{s} = 7$ TeV by the ATLAS Collaboration [3] and at $\sqrt{s} = 8$ TeV by both the ATLAS Collaboration [4] and the CMS Collaboration [5]. At 13 TeV, the ATLAS Collaboration has measured the t$\bar{\text{t}}\gamma$ production cross section in leptonic final states [6] and in the $e\mu$ final state [7]. All of these results are in agreement with the SM predictions within uncertainties.

In this report, the inclusive and differential production cross section of a top quark-antiquark pair and a photon (t$\bar{\text{t}}\gamma$) is measured in pp collisions at $\sqrt{s} = 13$ TeV. The analysis uses a data sample recorded by the CMS detector during Run II (2016–2018) of the LHC which corresponds to an integrated luminosity of 137 fb^{-1}. The measurement is performed in the semileptonic (e + jets, μ + jets) decay channels. Examples of Feynman diagrams at leading order (LO) contributing to the t$\bar{\text{t}}\gamma$ signal topology are shown in Fig. 1.

The inclusive and differential cross sections are obtained from a profiled log-likelihood fit using in-situ measurements of backgrounds with promptly produced photons (Zγ, Wγ), a background component with electrons misidentified as photons, and of photons produced via the fragmentation or hadronization of particles inside hadronic jets (nonprompt and misidentified photons). The promptly produced background contributions are separated from the signal by requirements on the multiplicity of jets and b-tagged jets, as well as the invariant mass of the lepton and the photon, $m(\ell, \gamma)$. The background component with misidentified photons originating from electrons is measured in a data sample comprising events where $m(e, \gamma)$ is close to the Z boson mass. The contribution from photons that originate from particles in hadronic jets is estimated in a data sample where photon identification and isolation requirements are relaxed. The inclusive t$\bar{\text{t}}\gamma$ cross section is measured for a selection on the transverse photon momentum, $p_T(\gamma)$, of $p_T(\gamma) > 20$ GeV. Differential cross sections are measured for $p_T(\gamma)$, $|\eta(\gamma)|$ and the angular separation of the lepton and the photon, $\Delta R(\ell, \gamma)$, and unfolded to a fiducial phase space volume defined at the particle level.

Anomalous top quark electroweak dipole moments predict modifications of the $t\gamma$ interaction. The results are interpreted in the context of SM effective field theory (SMEFT) [8], where the c_{tZ} and c_{tZ}^{I} operators defined in Ref. [9] are constrained using the measurement of the distribution of $p_T(\gamma)$ at the detector level.

This report is organized as follows. Details on the simulation of the signal and background processes and their modeling are provided in Section 2. The online selection, event reconstruction, and object definitions are described in Section 3. The event selection and the photon categorization are described in Section 4. The procedures to obtain background predictions are discussed in Section 5. Systematic uncertainties are discussed in Section 6 and the obtained results are presented in Section 7. The interpretation of the findings in the context of effective field theory is given in Section 8. Finally, a summary is provided in Section 9.

2 Simulated event samples

Simulated samples matching the varying conditions for each data taking period are generated using Monte Carlo event generators (MC). The $t\bar{t}\gamma$ signal events are generated with MADGRAPH5_aMC@NLO v2.6.5 [10] at leading order (LO) in perturbative quantum chromodynamics (QCD), and the cross section is rescaled to next-to-leading order (NLO). A global scale factor of 1.4852, computed with MADGRAPH5_aMC@NLO, corrects the inclusive cross section to the NLO one. The $t\bar{t}$, t-channel single-top-quark, tW and WW background processes are simulated at NLO with the POWHEG v2 [11–16] event generator while the other background processes are simulated with MADGRAPH5_aMC@NLO at LO or NLO. The $t\bar{t}$ simulation is normalized to a cross section of 832 pb calculated with the TOP++ (version 2.0) program [17] at NNLO including resummation of next-to-next-to-leading-logarithm (NNLL) soft-gluon terms and the proton structure described by the CT14 NNLO PDF set [18]. The relative uncertainty in this cross section is evaluated at 5%.

Events with $s-$ or $t-$ channel single top quarks produced are normalized to NLO cross sections [19, 20], while the normalizations of WW and tW are at NNLO [21]. Drell–Yan and W+ jets events are generated with up to four extra partons in the matrix element calculations with MADGRAPH5_aMC@NLO at LO and are normalized to NNLO cross sections [22–24] including electroweak corrections at NLO [25, 26]. The $t\bar{t}Z$, $t\bar{t}W$, tZq, $t\gamma$, $W\gamma$, $Z\gamma$, and other diboson processes (VV, with V either W or Z) are normalized to the most precise available NLO cross sections [27, 28]. In the following, to simplify the notation, the single-top, $t\bar{t}$, and $t\gamma$ processes are grouped in the $t/t\bar{t}$ category, and, furthermore, the tZq, $t\bar{t}W$, $t\bar{t}Z$, WW, WZ, and ZZ processes in a category labeled "other". A summary of the event samples is provided in Table 1.

The event generators are interfaced with PYTHIA v8.226 (8.230) [36] using the CP5 tune [37–39] for 2016 (2017, 2018) samples to simulate multi-parton interactions, fragmentation, parton shower, and hadronization of partons in the initial and final states, along with the underlying event. For the 2016 data taking period, the CUETP8M1 tune is used for the Drell–Yan, W+ jets, $t\gamma$, $W\gamma$, diboson, $t\bar{t}W$, and $t\bar{t}Z$ processes. The NNPDF parton distribution functions (PDFs) at different perturbative orders in QCD are used in v3.0 [40] and v3.1 [41] for 2016 and 2017–18 samples, respectively. Double counting of the partons generated with MADGRAPH5_aMC@NLO and PYTHIA is removed using the MLM [42] and the FXFX [43] matching schemes for LO and NLO samples, respectively. The events are subsequently processed with a GEANT4-based simulation model [44] of the CMS detector. All simulated samples include the effects of additional pp collisions in the same or adjacent bunch crossings (pileup), and are reweighted according to

Table 1: Event generator and orders of accuracy for each simulated process.

Process	Cross section normalization	Event generator	Perturbative order in QCD
$t\bar{t}\gamma$	NLO	MADGRAPH5_aMC@NLO	LO
$t\bar{t}$	NNLO+NNLL [17, 29–34]	POWHEG	NLO
single-t (t-channel)	NLO [19, 20]	POWHEG	NLO
single-t (s-channel)	NLO [19, 20]	MADGRAPH5_aMC@NLO	NLO
tW	NNLO [21]	POWHEG	NLO
Drell–Yan, W+ jets	NNLO [22–26]	MADGRAPH5_aMC@NLO	LO
$W\gamma$	NLO	MADGRAPH5_aMC@NLO	LO
WW	NNLO [35]	POWHEG	NLO
$t\gamma$, $Z\gamma$, WZ, ZZ $t\bar{t}Z$, $t\bar{t}W$, tZq	NLO	MADGRAPH5_aMC@NLO	NLO
multijet	LO	PYTHIA	LO

the distribution of the number of interactions in each bunch crossing corresponding to a total inelastic pp cross section of 69.2 mb [45].

3 Event reconstruction

Events are selected at the HLT level by trigger algorithms that require the presence of at least one lepton. The threshold on the transverse momentum (p_T) of the leading lepton is 27 GeV (electron) or 24 GeV (muon). In the 2017 LHC running period, the muon trigger threshold is raised to 27 GeV and in the 2017–2018 periods, the electron trigger threshold is raised to 32 GeV.

The particle-flow (PF) algorithm [46] aims to reconstruct and identify each individual particle in an event, with an optimized combination of information from the various elements of the CMS detector. The energy of photons is obtained from the ECAL measurement. Photon candidates are required to satisfy $p_T > 20$ GeV and fall within the barrel of the ECAL, $|\eta| < 1.4442$. The identification of photons is based on isolation and shower shape information as a function of p_T and η, and taking into account pileup effects [47]. In particular, the lateral shower extension ($\sigma_{\eta\eta}$) [48] must satisfy $\sigma_{\eta\eta} < 0.01015$.

The primary interaction vertex (PV) is chosen to have the largest value of summed physics-object p_T^2, where these physics objects are reconstructed by a jet-finding algorithm [49, 50] applied to all charged tracks associated with the vertex. The reconstruction and selection efficiency for photons in MC is corrected as a function of the p_T and η of the reconstructed photon to match the efficiency observed in data [51]. The energy of electrons is determined from a combination of the electron momentum at the PV, the energy of the corresponding ECAL cluster, and the energy sum of all bremsstrahlung photons spatially compatible with originating from the electron track. Electron candidates are required to satisfy $p_T > 35$ GeV and $|\eta| < 2.4$, excluding the transition region between the barrel and endcap of the ECAL, $1.4442 < |\eta| < 1.566$. The momentum of muons is obtained from the curvature of the corresponding track. Muon candidates are selected having $p_T > 30$ GeV and $|\eta| < 2.4$. The energy of charged hadrons is determined from a combination of their momentum measured in the tracker and the matching ECAL and HCAL energy deposits, corrected for zero-suppression effects and for the response function of the calorimeters to hadronic showers. Finally, the energy of neutral hadrons is obtained from the corresponding corrected ECAL and HCAL energy.

All lepton and photon candidates are required to be isolated from other objects by selecting

the reconstructed charged and neutral PF candidates in a cone around the candidate. A radius $\Delta R = \sqrt{(\Delta\eta)^2 + (\Delta\phi)^2} = 0.4\,(0.3)$ is used for muon candidates (electron or photon candidates) where ϕ is the azimuthal angle in radians. A muon candidate is isolated if the pileup corrected scalar p_{T} sum of photons and neutral and charged hadrons reconstructed by the PF algorithm within this cone is less than 15% of the lepton p_{T}, i.e. $I_{\mathrm{rel}}(\mu) < 0.15$. For electron candidates, p_{T} and η dependent thresholds are set on $I_{\mathrm{rel}}(e)$ in the range of 5%–10% and a total selection efficiency of 80% is achieved for this working point. A "veto electron ID" is defined with a $I_{\mathrm{rel}}(e)$ of 25% and is found 95% efficient. For photon candidates, the scalar p_{T} sum of the charged particles within a cone of $\Delta R \leq 0.3$, the charged photon isolation ($I_{ch.}$), must satisfy $I_{ch.} \leq 1.141$ GeV. Depending on the photon candidate p_{T}, there are separate requirements on the neutral hadrons and photon isolation.

Jets are reconstructed by clustering PF candidates using the anti-k_{T} algorithm with a distance parameter of 0.4. Selected jets are required to satisfy $p_{\mathrm{T}} > 30\,\mathrm{GeV}$ and $|\eta| < 2.4$. Contribution to the clustered energy from pileup interactions is corrected for by requiring charged-hadron candidates to be associated with the PV and an offset correction for the contribution from neutral hadrons falling within the jet area is subtracted from the jet energy. Corrections to the jet energy scale (JES) are applied in simulation and data. The jet energy resolution (JER) is corrected in simulation to match the resolution observed in data [52].

The missing transverse momentum vector, $\vec{p}_{\mathrm{T}}^{\,\mathrm{miss}}$, is defined as the projection onto the plane perpendicular to the beams of the negative vector momentum sum of all PF candidates in an event. The jet energy scale and resolution corrections are included in the $\vec{p}_{\mathrm{T}}^{\,\mathrm{miss}}$ computation. Its magnitude is referred to as $p_{\mathrm{T}}^{\mathrm{miss}}$.

Jets originating from the hadronization of a b quark are identified with a deep neural network algorithm [53] based on tracking and secondary vertex information (b tagged). A working point is chosen such that the efficiency to identify a b jet is 55-70% for a jet p_{T} between 20 and 400 GeV. The misidentification rate in this p_{T} range is 1-2% for light jets and up to 12% for charm quark jets. A correction is applied to the simulation to match the b tagging efficiencies observed in data.

4 Event selection

4.1 Reconstruction level

The measurement is conducted in a signal region with exactly one lepton ($N_\ell = 1$), exactly one photon ($N_\gamma = 1$), and three or more jets ($N_{\mathrm{jet}} \geq 3$) among which at least one is b-tagged ($N_{\mathrm{b\,jet}} \geq 1$). The observable M_3 is computed as the 3-jet invariant mass of the jet combination that maximizes the magnitude of the transverse momentum vector sum. For the extraction of the inclusive cross section, the $p_T(\gamma) > 20$ GeV signal region is binned in 3 bins M_3 in the ranges 0–280, 280–420 and >420 GeV. The side band and validation regions employed in the background estimation procedures, as well as the signal regions, are summarized in Table 2. A detailed discussion of the signal and control regions is given in Sec. 5.

After the event selection, a significant portion of the background events comes from processes with a nonprompt or misreconstructed photon (19.2%) or misidentified electron (17.3%). Based on a matching between simulated particles and the reconstructed photon, events are categorized according to the origin of the reconstructed photon in the event. Reconstructed photons are matched to the generator level particles from the primary interaction with the smallest ΔR if a threshold $\Delta R < 0.3$ is satisfied, and if the transverse momentum of the photon is within

Table 2: Overview of signal and control regions. For ZG, WG, and misDY the regions with suffixes 3 (4p) have a modified jet multiplicity requirement of $N_{\text{jet}} = 3$ ($N_{\text{jet}} \geq 4$).

Region	N_ℓ	N_{jet}	$N_{\text{b jet}}$	N_γ	other requirements
QCD_{2j0b}	1	2	0	0	
ZG3p	1	≥ 3	0	1	$m(e,\gamma) < m_Z - 10$ $m(\mu,\gamma) < m_Z$
WG3p	1	≥ 3	0	1	$m(e,\gamma) > m_Z + 10$ $m(\mu,\gamma) > m_Z$
misDY3p	1	≥ 3	0	1	$\lvert m(e,\gamma) - m_Z \rvert < 10$
SR3p	1	≥ 3	≥ 1	1	

50% to the one of the matched particle.

4.2 Photon classification

Events are subsequently classified into one of three categories based on the matched generator particle. In the "genuine photon" category, the reconstructed photon is matched to a generated photon that originates from a lepton, a boson, or a quark. The "hadronic photon" category is comprised of events where the photon is matched to a generated photon that originates from a hadron (71.2%), or if no photon match is found at all, thus including a contribution with misidentified photons (28.8%). This category thus also contains a small contribution from photons that originate from pileup interactions. In the "misidentified electron" category, the photon is matched to an electron.

4.3 Fiducial phase space definition

The fiducial region of the analysis is defined at particle level by applying a similar event selection to the stable particles after the event generation, parton showering and hadronization but before the detector simulation. Electrons (muons) must have $p_{\text{T}} > 35\ (30)$ GeV and $|\eta| < 2.4$ and must not originate from hadron decays. Photons are selected if they do not originate from hadron decays, satisfy $p_{\text{T}} > 20$ GeV and $|\eta| < 1.4442$, and are found outside a cone of $\Delta R > 0.4$ around the leptons. Photons inside a cone of $\Delta R \leq 0.1$ are added to the lepton before the lepton selection. The photon must be isolated from all stable particles except neutrinos with a $p_T > 5$ GeV. Jets are clustered using the anti-kt algorithm with $R = 0.4$ using all final state particles excluding neutrinos. Jets must have $p_{\text{T}} > 30$ GeV and $|\eta| < 2.4$. A ghost matching method [54] to b hadrons is used to determine the flavour of the jets, with those matched to b hadrons tagged as b jets. Finally, the overlap of jets and other candidates is removed by excluding jets within $\Delta R \leq 0.4$ of lepton candidates or within $\Delta R \leq 0.1$ of photon candidates. Using these definitions, the fiducial region is constructed by requiring exactly one photon, exactly one lepton, and three or more jets among which at least one is b-tagged.

5 Background estimation

The $\text{t}\bar{\text{t}}\gamma$ process typically produces events with large jet and b-tagged jet multiplicities and an isolated photon with large p_{T}. Several background processes can mimic the signal and their contributions to the signal regions are estimated using background enriched control regions.

Events with $N_{\text{b jet}} = 0$ are dominated by backgrounds with promptly produced photons ($\text{Z}\gamma$,

Wγ). Using the invariant mass of the lepton and the photon ($m(\ell,\gamma)$), a further significant component of backgrounds with misidentified electrons can be separated from the prompt backgrounds and these contributions are normalized in-situ. A background from photons produced via the fragmentation or hadronization of particles inside hadronic jets (nonprompt photons) is estimated in a control region with relaxed criteria on $I_{ch.}$ and $\sigma_{\eta\eta}$. The QCD multijet background with misidentified or nonprompt leptons is estimated by normalizing suitable templates obtained from an event sample with leptons passing loose lepton isolation criteria.

The separation between signal and backgrounds is obtained from a binned maximum-likelihood fit. In order to extract the $p_T(\gamma)$ dependence of the background with misidentified electrons, the misDY control region is split into 7 bins separated by the thresholds 20, 35, 50, 65, 80, 120, 160 and ∞ GeV. The WG and ZG control regions are similarly separated into 3 bins defined by the thresholds 20, 65, 160 and ∞ GeV. Because the dependence of the scale factors on $|\eta(\gamma)|$ and $\Delta R(\ell,\gamma)$ is negligible, this choice is kept in all measurements. In the fit, the contributions from the various background processes are allowed to vary within their uncertainties. The normalizations of the contribution with misidentified electrons and the Wγ process are left floating. Figure 2 shows some kinematic distributions in the SR3p selection where the simulated event samples are categorized according to the photon and for post-fit values of the nuisance parameters.

5.1 QCD multijet background

Since the probability for a simulated multijet event to mimic the final state of the signal process is very small, it becomes impractical to simulate a sufficiently large number of events for this background. Therefore, the background from multijet events, comprising events with misidentified and non-prompt leptons, is estimated in a staged procedure based on data in side band regions with loosened isolation criteria for each given N_{jet}, $N_{\text{b jet}}$, and N_γ. In the muon channel, the side band region is defined by loosening the muon isolation requirement to $I_{\text{rel}}(\mu) < 0.25$, while for the electron channel the isolation criterion is loosened to the veto electron ID working point. Events with leptons satisfying the nominal isolation criteria are removed. This selection results in a region dominated by multijet events.

Next, a transfer factor ("TF") is measured in the $N_{\text{jet}} = 2$, $N_\gamma = 0$ selection (QCD_{2j0b}) as the ratio of the multijet event yield with tightly isolated lepton candidates to the yield with loosely isolated lepton candidates. The measurement is performed by fitting a template in the transverse W boson candidate mass, calculated from the formula

$$m_{\text{T}}(\text{W}) = \sqrt{2p_{\text{T}}^{\ell} p_{\text{T}}^{\text{miss}} \left[1 - \cos(\phi^{\ell} - \phi^{\text{miss}})\right]} \tag{1}$$

using the p_{T} and the azimuthal angle ϕ of the charged lepton and $\vec{p}_{\text{T}}^{\,\text{miss}}$. The template is taken from data, subtracting the electroweak background, in a selection with loosely isolated leptons and with $N_{\text{b jet}} = 0$. A fit to the observed $m_{\text{T}}(\text{W})$ distribution in the selection with tightly isolated leptons and the nominal $N_{\text{b jet}} = 0$ requirement is performed to extract the TF. The template fit result in the QCD_{2j0b} region is shown in Fig. 3.

A correction based on simulated multijet events is applied to account for the TF dependence on N_{jet}. Because the efficiency of the tight lepton selection in multijet events depends on p_{T} and η of the lepton, the estimation procedure is performed in a total of 24 bins defined in these observables. Depending on p_{T} and η of the lepton, the TF vary in the range of 0.9–3.1 (0.1–0.3) for $N_{\text{b jet}} = 0$ (≥ 1) for the e channel and 2.0–3.7 (0.6–1.0) for the μ channel. Finally, the multijet estimate is obtained by multiplying the side band yields with loosely isolated leptons with the

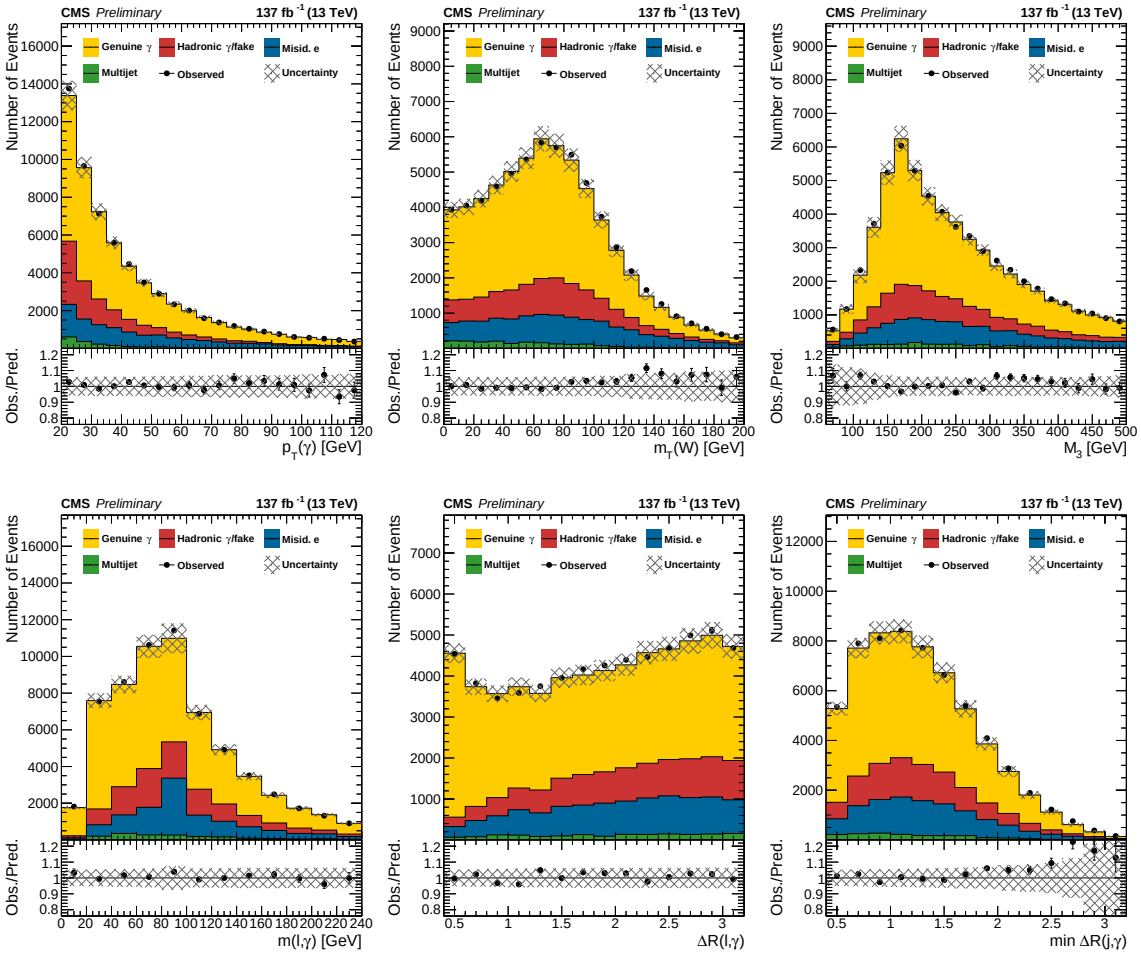

Figure 2: Distribution of $p_T(\gamma)$, the transverse mass $m_{\mathrm{T}}(\mathrm{W})$ of the W boson candidate, the three-jet invariant mass M_3 (upper row) and the invariant mass of the lepton and the photon ($m(\ell,\gamma)$), the angular separation of the lepton and the photon ($\Delta R(\ell,\gamma)$), and the angular separation of the leading jet and the photon ($\Delta R(j_1,\gamma)$) (lower row). The lower panels show the ratio of the observation to the prediction. The systematic uncertainties are shown as a shaded band.

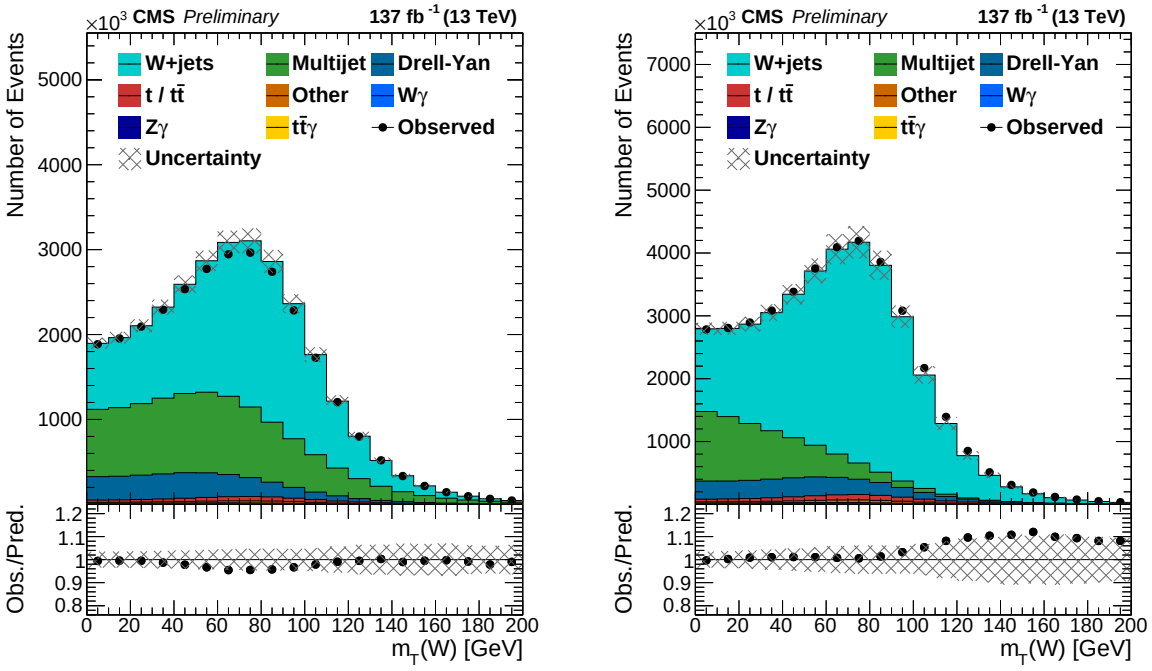

Figure 3: Fit result of the multijet template obtained with loosely isolated leptons and the electroweak background to the measured $m_{\mathrm{T}}(\mathrm{W})$ distribution with isolated leptons in the $N_{\text{jet}} = 2$, $N_{\text{b jet}} = 0$ selection for electrons (left) and muons (right). The lower panels show the ratio of the observation to the prediction. The systematic uncertainties are shown as a shaded band.

TF estimates and summing the predictions in these bins. It is estimated at 8% (12%) in the μ (e) channel in the ZG3p and WG3p control regions and below 0.5% in the signal regions.

5.2 Hadronic photon background

For the estimation of the background component with hadronic photons, the weak correlation of $\sigma_{\eta\eta}$ with $I_{ch.}$ is exploited in an ABCD method. In a side band with a requirement of $\sigma_{\eta\eta} \geq 0.011$ on the photon candidate, the expected yield with genuine photons is subtracted. It is used to obtain r_{SB}, defined as the ratio of the yield passing the $I_{ch.} < 1.141$ GeV requirement to the event yield failing it. The estimation is obtained by multiplying r_{SB} with the yield in the corresponding normalization region, defined by the nominal $\sigma_{\eta\eta}$ requirement and $I_{ch.} > 1.141$ GeV. A small correlation between the two observables is corrected based on simulation.

5.3 Misidentified electron and genuine photon backgrounds

The background from electrons that are mis-identified as photons is obtained from control regions with a $|m(e,\gamma) - m_{\mathrm{Z}}| < 10$ requirement and exactly three (misDY3) and four or more (misDY4p) jets. This event sample is enriched by Drell–Yan events with $\mathrm{Z} \to ee$, where one of the electrons passes the photon selection criteria and can thus be used to extract a scale factor (SF) for the background component with misidentified electrons. Because of differences in the detector configurations, this measurement is performed separately for the three data taking periods.

The $\mathrm{W}\gamma$ and $\mathrm{Z}\gamma$ processes also contribute to this sample, but the distribution of the $m(\ell,\gamma)$ observable does not peak in the vicinity of m_{Z} for these backgrounds. The SF for these processes are obtained from the ZG3, modified ZG4p, WG3, and WG4p regions by performing a profiled

likelihood fit, including also the data-driven estimate for multijet events. The resulting $m(\ell,\gamma)$ distributions are shown in Fig. 4. A correction of 15% to the normalization of the Drell–Yan process is measured in an event sample with two well identified leptons satisfying $|m(\ell,\ell) - m_Z| < 10$ and $N_{\text{jet}} \geq 3$. It is included in these results. A summary of the extracted SF is provided in Tab. 3. The observed changes in the SF for misidentified electrons are a result of the replacement of the pixel detector in 2017 and its performance in the three data taking periods.

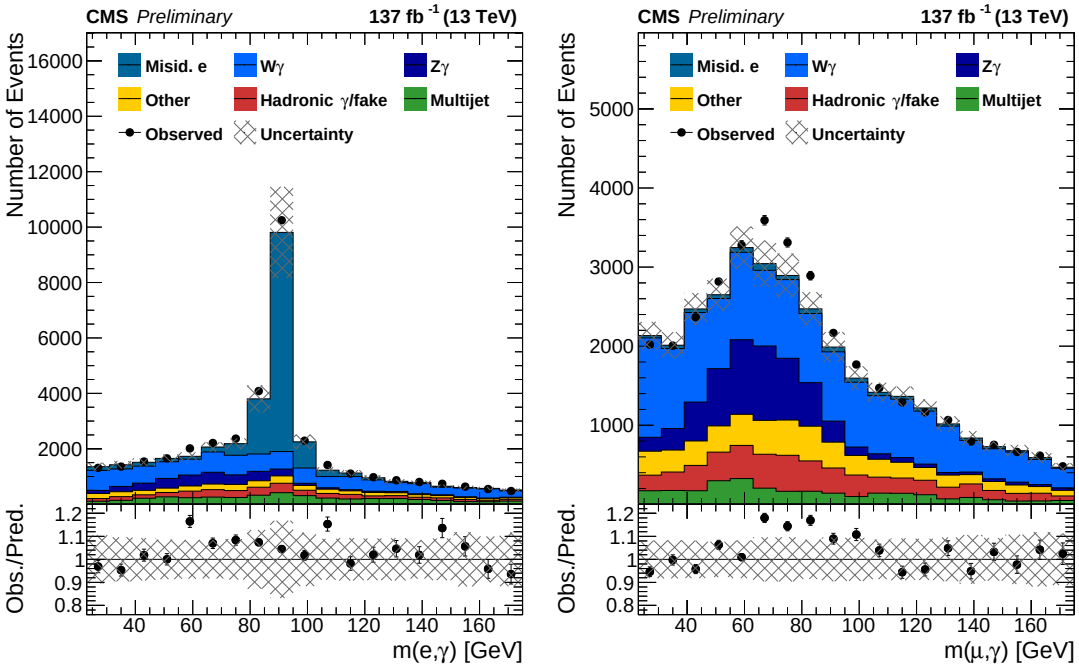

Figure 4: Distribution of the invariant mass of the lepton and the photon ($m(\ell,\gamma)$) in the $N_{\text{jet}} \geq 3$, $N_{\text{b jet}} = 0$ selection for the e channel (left) and the μ channel (right). The lower panels show the ratio of the observation to the prediction. The systematic uncertainties are shown as a shaded band.

Table 3: Extracted scale factors for the contribution from misidentified electrons for the three data taking periods, and the $Z\gamma$, $W\gamma$ scale factors.

scale factor	value
misidentified e 2016	2.22 ± 0.28
misidentified e 2017	1.83 ± 0.24
misidentified e 2018	1.59 ± 0.18
$Z\gamma$ normalization	0.83 ± 0.10
$W\gamma$ normalization	1.20 ± 0.09

The stability of the procedure is assessed by repeating the fit on individual data taking periods and separately for the $N_{\text{jet}} = 3$ and $N_{\text{jet}} \geq 4$ selections. The extracted scale factors agree within uncertainties.

6 Systematic uncertainties

The systematic uncertainties affecting the signal selection efficiency and background yields are summarized in Table 4. The table shows the range of variations in the different bins of the analysis caused by each systematic uncertainty on the signal and background yields, as well as an estimate of the impact of each input uncertainty on the measured inclusive cross section. The table also indicates whether the uncertainties are treated as uncorrelated or fully correlated among the data taking periods.

The uncertainty in the integrated luminosity is 2.3–2.5% [55–57]. Simulated events are reweighted according to the distribution of the number of interactions in each bunch crossing corresponding to a total inelastic pp cross section of 69.2 mb [45]. The uncertainty in the total inelastic pp cross section is 4.6% [58] and affects the pileup estimate. The uncertainty in the expected yields is about 2%.

The uncertainties in the corrections to the trigger selection efficiencies are propagated to the results. These efficiencies are measured in data samples with an independent trigger selection and compared to those obtained in simulation. A 0.5% uncertainty is assigned to the yields obtained in simulation. Lepton selection efficiencies are measured using a "tag-and-probe" method [47, 59] in bins of lepton p_{T} and η, and are found to be in the range 75–85% (50–80%) for muons (electrons). These measurements are performed separately in data and simulation. The differences between these two measurements are used to scale the yields obtained in the simulation. The impact of these uncertainties is 0.7% (0.5%) for the muon (electron) channel.

In the barrel section of the ECAL, an energy resolution of about 1% is achieved for unconverted or late-converting highly energetic photons. The remaining barrel photons have a resolution of about 1.3% up to $|\eta| = 1$, rising to about 2.5% at $|\eta| = 1.4$. Uncertainties in the photon energy scale and resolution are measured with electrons from Z boson decays, reconstructed using information exclusively from the ECAL [48, 51]. Additionally, an event sample enriched in $\mu^+\mu^-\gamma$ events is used to measure a scale factor correcting the efficiency of the electron veto [60]. The total uncertainty in the photon energy and identification amounts to 1.4% for the inclusive cross section and reaches 2% for $p_T(\gamma) \geq 100\,\mathrm{GeV}$.

Uncertainties in the jet energy calibration are estimated by shifting the jet energy corrections in simulation up and down by one standard deviation. Depending on p_{T} and η, the uncertainty in jet energy scale varies in the range 2–5% [52], leading to uncertainties in the predicted signal and background yields of 1.0–4.1% and an impact on the inclusive cross section of 1.9%. For the signal and backgrounds modeled via simulation, the uncertainty in the measurement is determined from the observed differences in the yields with and without the shift in jet energy corrections. The same technique is used to calculate the uncertainties from the jet energy resolution, which are found to be less than 1% [52]. The b tagging efficiency in the simulation is corrected using scale factors determined from data [53, 61]. These are estimated separately for correctly and incorrectly identified jets, and each results in an uncertainty of about 0.8–1.6% on the yields in the signal regions, depending on $N_{\mathrm{b\,jet}}$.

During the 2016 and 2017 data-taking periods, a gradual shift in the timing of the inputs of the ECAL L1 trigger in the forward endcap region ($|\eta| > 2.4$) led to a specific inefficiency (labelled L1 prefiring in Tab 4). A correction for this effect was determined using an unbiased data sample and is found to be relevant in events with high-p_{T} jets with $2.4 < |\eta| < 3.0$. While no reconstructed objects at this pseudorapidity enter the measurements, the systematic variation of 20% of this correction for affected events nevertheless leads to a subleading uncertainty of 0.3–0.9% on the predicted yields.

To estimate the theoretical uncertainties from missing higher-order corrections, the choice of μ_R and μ_F is varied independently up and down by a factor of 2, ignoring the case, in which one parameter is scaled up while the other is scaled down. The envelope of the acceptance variations is taken as the systematic uncertainty in each bin before the profiled likelihood fit and is found to be smaller than 4.7%. The different sets in the NNPDF PDF [40] are used to estimate the corresponding uncertainty in the acceptance for the cross section measurement, which is less than 0.5%. The uncertainty associated with the choice of PDFs for the anomalous coupling and SMEFT interpretations is estimated by using several PDFs and assigning the maximum differences as the quoted uncertainty, following the PDF4LHC prescription with the MSTW2008 68% CL NNLO, CT10 NNLO, and NNPDF2.3 5f FFN PDF sets (as described in Ref. [62] and references therein, as well as Refs. [63–65]). The scale and PDF uncertainties in the fiducial cross section of the $\mathrm{t\bar{t}}\gamma$ process amount to 18%. In the parton shower simulation, the uncertainty from the choice of μ_F is estimated by varying the scale of initial- (ISR) and final-state radiation (FSR) up by factors of 2 and $\sqrt{2}$ and down by factors of 0.5 and $1/\sqrt{2}$, respectively, as suggested in Ref. [37]. The default configuration in PYTHIA includes a model of color reconnection based on multiple parton interactions (MPI) with early resonance decays switched off. To estimate the uncertainty from this choice of model, the analysis is repeated with three other color reconnection models within PYTHIA: the MPI-based scheme with early resonance decays switched on, a gluon-move scheme [66], and a QCD-inspired scheme [67]. The total uncertainty from color reconnection modeling is estimated by taking the maximum deviation from the nominal result and amounts to 0.6% on the inclusive cross section.

The uncertainty in the normalization of the QCD multijet component is based on the TF dependence for different $N_{\mathrm{b\,jet}}$ and independent uncertainties of 50% are assumed for the contributions to the $N_{\mathrm{b\,jet}} = 0$ and $N_{\mathrm{b\,jet}} \geq 1$ yields. These are significant only in the WG3p and ZG3p control regions and lead to an uncertainty of 0.9% in the measured cross section. The corresponding impact of the normalization of the $\mathrm{Z}\gamma$ and $\mathrm{W}\gamma$ contributions are 0.5% and 2.4%, respectively. The component with misidentified electrons leads to an uncertainty of up to 8% on the predicted background yields with an impact on the inclusive cross section of 1.8%. The normalization of the Drell–Yan process and other small background components leads to additional uncertainties below 1%.

7 Results

7.1 Inclusive cross section measurement

The observed data, as well as the predicted signal and background yields in the control and signal regions are shown in Fig. 5 and 6. The signal cross section is extracted from these categories using the statistical procedure detailed in Refs. [68, 69]. The observed yields, signal and background estimates in each analysis category, and the systematic uncertainties are used to construct a binned likelihood function $L(r, \theta)$ as a product of Poisson probabilities of all bins. As described in Section 6, the bins of the three data-taking periods are kept separate, and the correlation pattern of the uncertainty as specified in Table 4. The parameter r is the signal strength modifier, i.e., the ratio between the measured cross section and the central value of the cross section predicted by simulation, and θ represents the full suite of nuisance parameters.

The test statistic used in this report is the profile likelihood ratio, $q(r) = -2 \ln L(r, \hat{\theta}_{\mathrm{r}}) / L(\hat{r}, \hat{\theta})$, where $\hat{\theta}_{\mathrm{r}}$ reflects the values of the nuisance parameters that maximize the likelihood function for signal strength r. A multi-dimensional fit is used to extract the observed cross section of the signal process and the associated uncertainties [68, 69]. The quantities $\hat{r}$ and $\hat{\theta}$ are the values

Table 4: Summary of systematic uncertainties. The first column indicates the source of the uncertainty. The second column shows the correlation between the data taking periods, where the ✓ symbol indicates 100% correlation. The third column shows the typical pre-fit uncertainties in the simulated yields of the signal region. The last column gives the corresponding systematic uncertainty in the $t\bar{t}\gamma$ cross section using the fit result.

	Source	Correlation	Uncertainty (%)	
			yield	$\sigma(t\bar{t}\gamma)$
Experimental	Luminosity	partial	2.3-2.5	2.4
	Pileup	✓	< 2.0	< 0.5
	Trigger efficiency	–	0.1-0.5	< 0.5
	Muon reconstruction and identification	partial	0.5-0.7	0.7
	Electron reconstruction and identification	✓	0.2-1.7	< 0.5
	Photon reconstruction and identification	✓	0.4-1.4	1.0
	$p_T(e)$ and $p_T(\gamma)$ reconstruction	✓	<1.2	< 0.5
	JES	partial	1.0-4.1	1.9
	JER	–	0.4-1.6	0.6
	B-tagging	2017/2018	0.8-1.6	1.1
	L1 prefiring	2016/2017	0.3-0.9	< 0.5
Theoretical	Tune	✓	0.1-1.9	< 0.5
	Color reconnection	✓	0.4-3.6	0.6
	ISR/FSR	✓	1.0-5.6	1.9
	PDF	✓	< 0.5	< 0.5
	ME scales μ_r, μ_f	✓	0.4-4.7	< 0.5
Background	Multijet normalization	✓	1.3-6.5	0.9
	Misidentified γ estimation	✓	1.2-2.7	2.0
	$t\bar{t}$ normalization	✓	1.0-1.9	1.0
	Misidentified e	–	2.5-8.0	1.8
	$Z\gamma$ normalization	✓	0.6-2.5	0.5
	$W\gamma$ normalization	✓	1.0-3.5	2.4
	DY normalization	✓	0.1-1.1	1.0
	"Other" bkg. normalization	✓	0.3-1.0	< 0.5

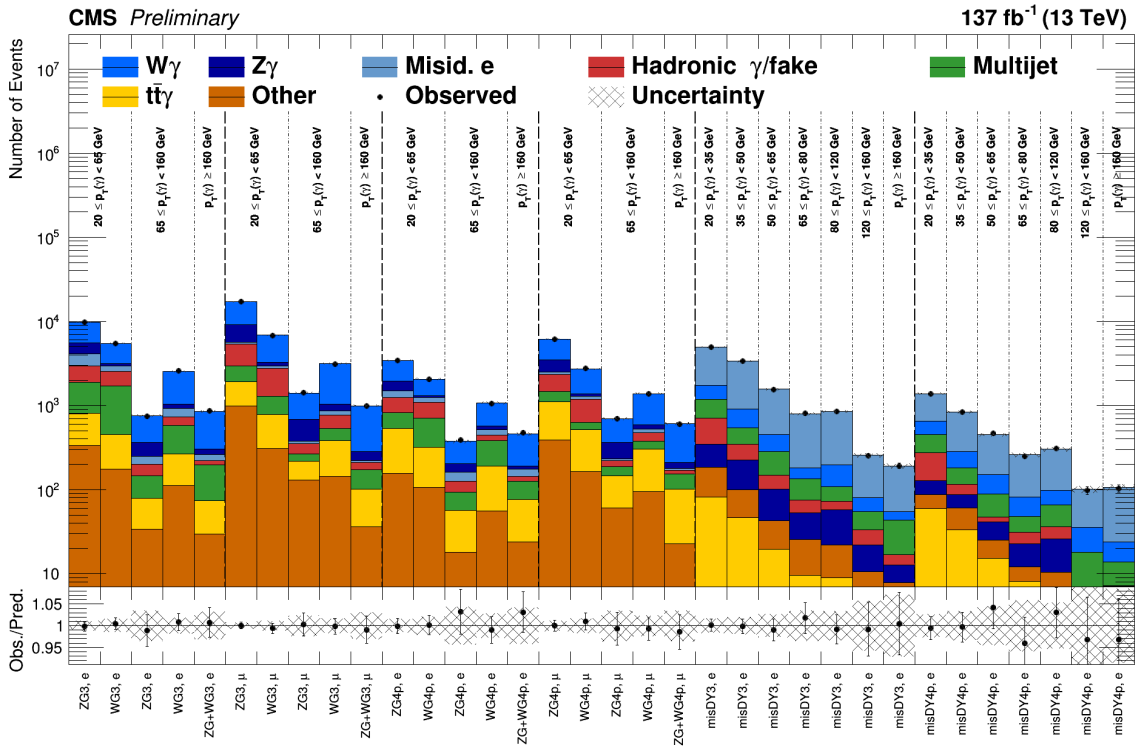

Figure 5: Predicted yields and observation in the control regions in the $N_{\text{jet}} = 3$ and $N_{\text{jet}} \geq 4$ selections for post-fit values of the nuisance parameters. The lower panels show the ratio of the observation to the prediction. The shaded bands show the systematic uncertainty in the background prediction.

that simultaneously maximize L. The fit is performed for the inclusive cross section measurements, and separately for the differential measurement. The nuisances related to experimental uncertainties and uncertainties in the modelling of signal and background processes are described by log-normal probability density functions. Nuisance parameters related to the normalization of the Wγ background and the background component with misidentified electrons is left floating in the fit. These rate parameters are complemented by nuisances for the normalization of the Zγ, the t$\bar{\text{t}}$ processes, and a nuisance for the normalization of other simulated backgrounds. Besides the extraction of the nuisance parameters related to normalization of background components, there are no significant constraints of other nuisance parameters. The normalization of the Wγ background is the largest individual contribution to the uncertainty in the inclusive cross section measurement.

A comparison of the measured cross sections and the SM prediction is shown in Figure 7. The combined cross section of the $N_{\text{jet}} = 3$ and $N_{\text{jet}} \geq 4$ channels within the fiducial phase space is measured to be

$$\sigma^{\text{fid.}}(\text{t}\bar{\text{t}}\gamma) = 800 \pm 46\,(\text{syst}) \pm 7\,(\text{stat})\,\text{fb} \tag{2}$$

7.2 Differential cross section measurement

The differential cross section is measured as a function of $p_T(\gamma)$, $|\eta(\gamma)|$, and $\Delta R(\ell, \gamma)$. Results are obtained simultaneously for the e and μ channels, the 3 jet and ≥ 4 jet bins, and for the three data taking periods. The binning of the differential distributions at the reconstruction level is shown in Table 5.

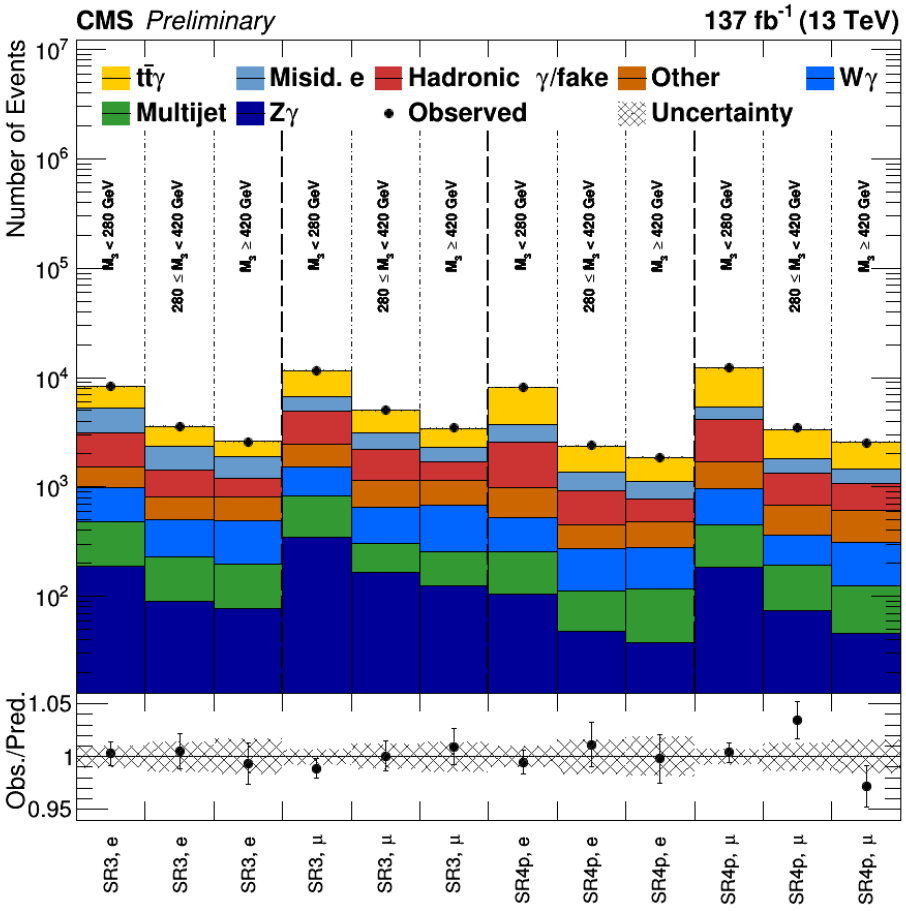

Figure 6: Predicted yields and observation in the signal regions in the $N_{\text{jet}} = 3$ and $N_{\text{jet}} \geq 4$ selections for post-fit values of the nuisance parameters. The lower panels show the ratio of the observation to the prediction. The systematic uncertainties are shown as a shaded band.

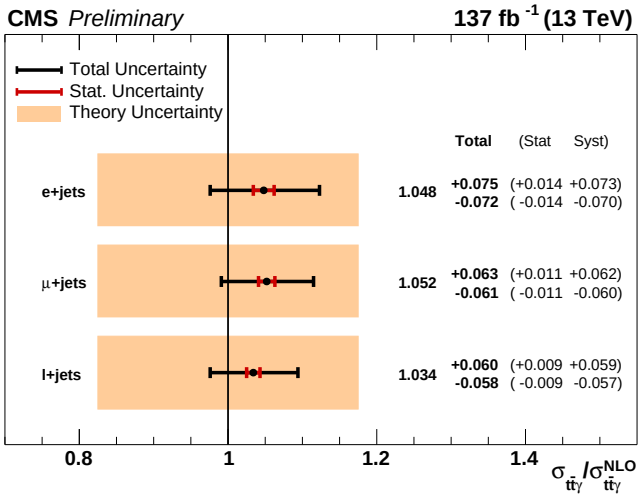

Figure 7: Summary of the measured cross sections normalized to the NLO cross section prediction for signal regions binned in the e-channel, μ-channel and the combined single lepton measurement. The light brown band indicates the theory uncertainty in the prediction.

Table 5: Binning choices in the differential measurements.

$p_T(\gamma)$	20, 35, 50, 65, 80, 100, 120, 140, 160, 200, 240, 280, ∞ GeV
$\Delta R(\ell, \gamma)$	0.4, 0.6, 0.8, 1.0, 1.2, 1.4, 1.6, 1.8, 2.0, 2.2, 2.4, 2.6, 2.8, 3.0, ∞
$\lvert\eta(\gamma)\rvert$	0, 0.15, 0.3, 0.45, 0.6, 0.75, 0.9, 1.05, 1.2, 1.35, 1.4442

For each bin, the signal strength is left floating in the profiled likelihood fit. The fit is performed separately for each distribution. The distributions of the observables after background subtraction are shown in Fig. 8.

These reconstruction level distributions are now unfolded to the fiducial particle level phase space defined in Sec. 4.3. In the simulation, the transverse momentum of the photon is taken as the final momentum after any QCD and electroweak radiation. The differential cross section is defined in the same phase space as the inclusive cross section reported above, i.e., in the phase space where the top quark pair is produced in association with a photon satisfying $p_T(\gamma) \geq 20$ GeV and $|\eta| < 1.4442$.

The $\mathrm{t\bar{t}}\gamma$ MADGRAPH5_aMC@NLO MC sample is used to construct a response matrix that takes into account both detector response and acceptance corrections. The same corrections, scale factors, and uncertainties as used in the inclusive cross section are applied. Because of the high photon momentum resolution, the fraction of events migrating from a specific momentum region at particle level to another one at detector level is small for all unfolded distributions. Under such conditions, no additional assumptions on the regularization of the unfolding method is required [70]. In this analysis, the `TUnfold` package [71] is used to obtain the results for the three measured observables.

Uncertainties in the estimated signal yields are propagated through the unfolding procedure, including the effects on the response matrix. Experimental uncertainties from the detector response and efficiency, such as the photon identification, jet energy scale, and b tagging uncertainties, are applied as a function of the reconstructed observable. The differential cross sections, obtained by this procedure, are shown in Fig. 9. For $p_T(\gamma) > 120\,\mathrm{GeV}$, the uncertainties in the JES, the photon identification efficiency, and the color reconnection modeling are the largest sources of uncertainty. The covariance matrices of the unfolded differential measurements are shown in Fig. 10. Including the scale and PDF uncertainties in the fiducial signal cross section, the corresponding χ^2 test statistic is 8.3 with 8 degrees of freedom (d.o.f.) for the $p_T(\gamma)$ distribution, 3.8 with 5 d.o.f. for $|\eta(\gamma)|$, and 6.8 with 7 d.o.f. for $\Delta R(\ell, \gamma)$.

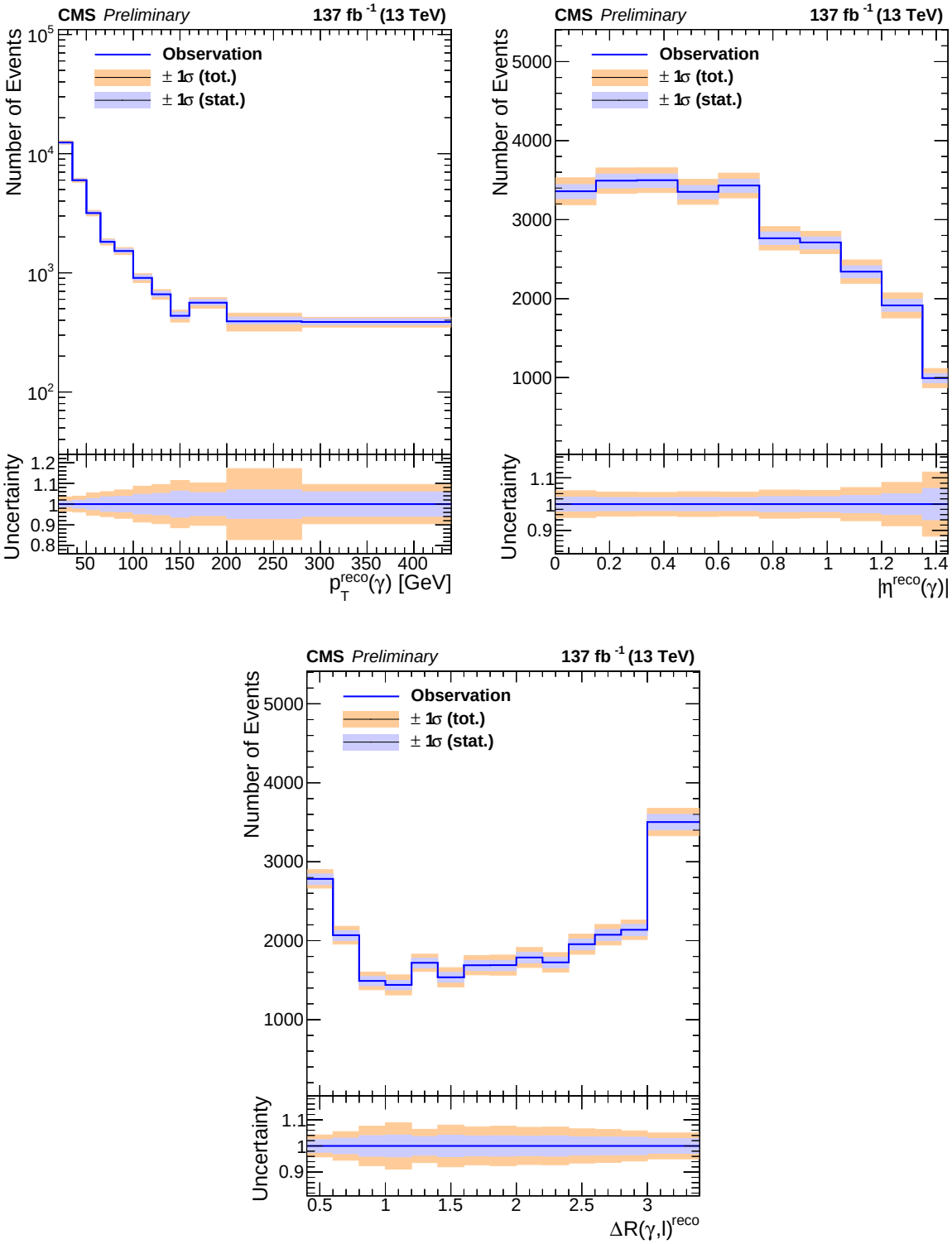

Figure 8: The distribution of $p_T(\gamma)$ (left), $|\eta(\gamma)|$ (right), and $\Delta R(\ell, \gamma)$ (bottom) in the $N_{\text{jet}} \geq 3$ selection after background subtraction. The lower panel displays the relative uncertainty, where the inner and outer bands show the statistical and total uncertainties, respectively.

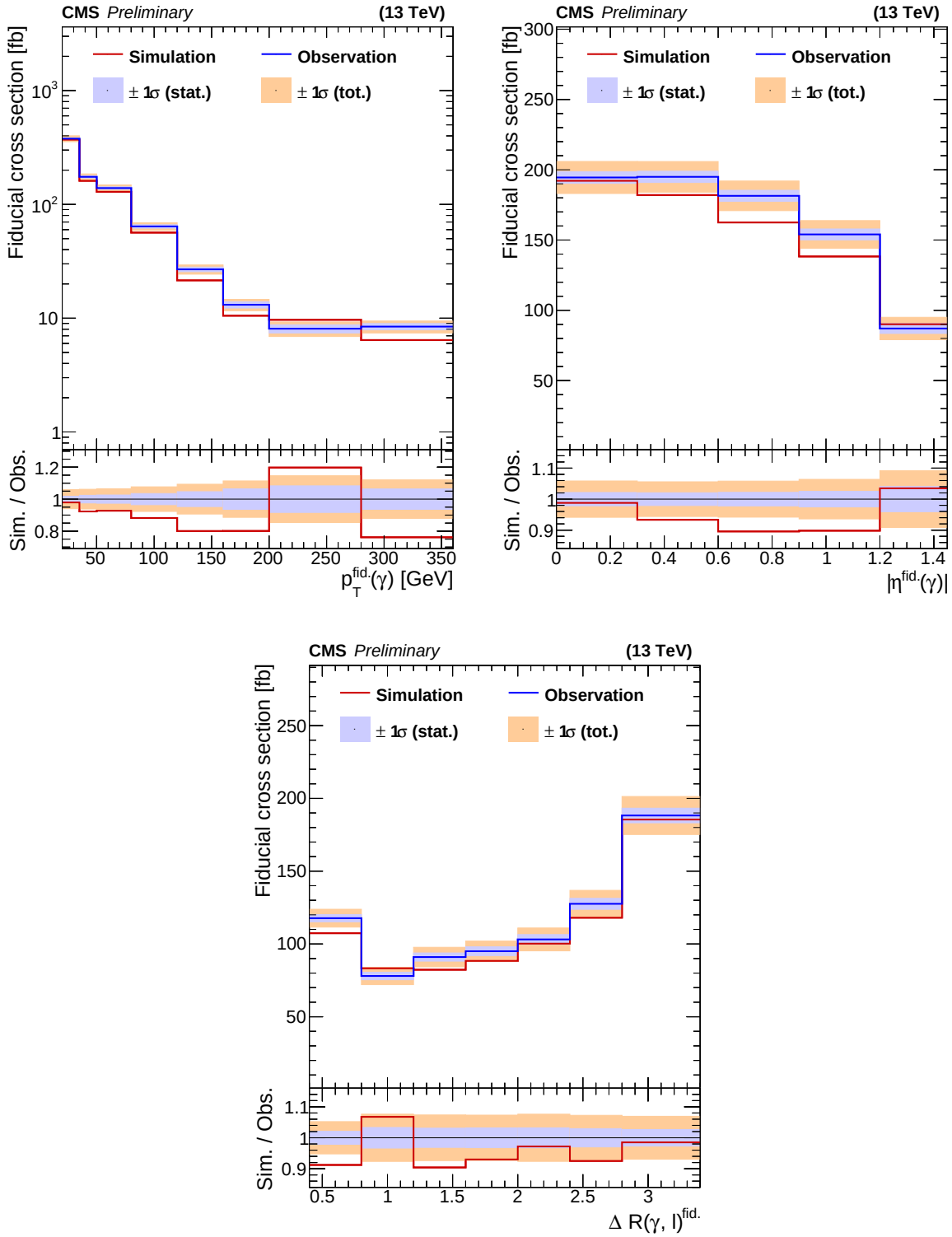

Figure 9: The unfolded differential cross sections for $p_T(\gamma)$ (left), $|\eta(\gamma)|$ (right), and $\Delta R(\ell, \gamma)$ (bottom). The lower panel displays the ratio of simulation to the observation. The inner and outer bands show the statistical and total uncertainties, respectively.

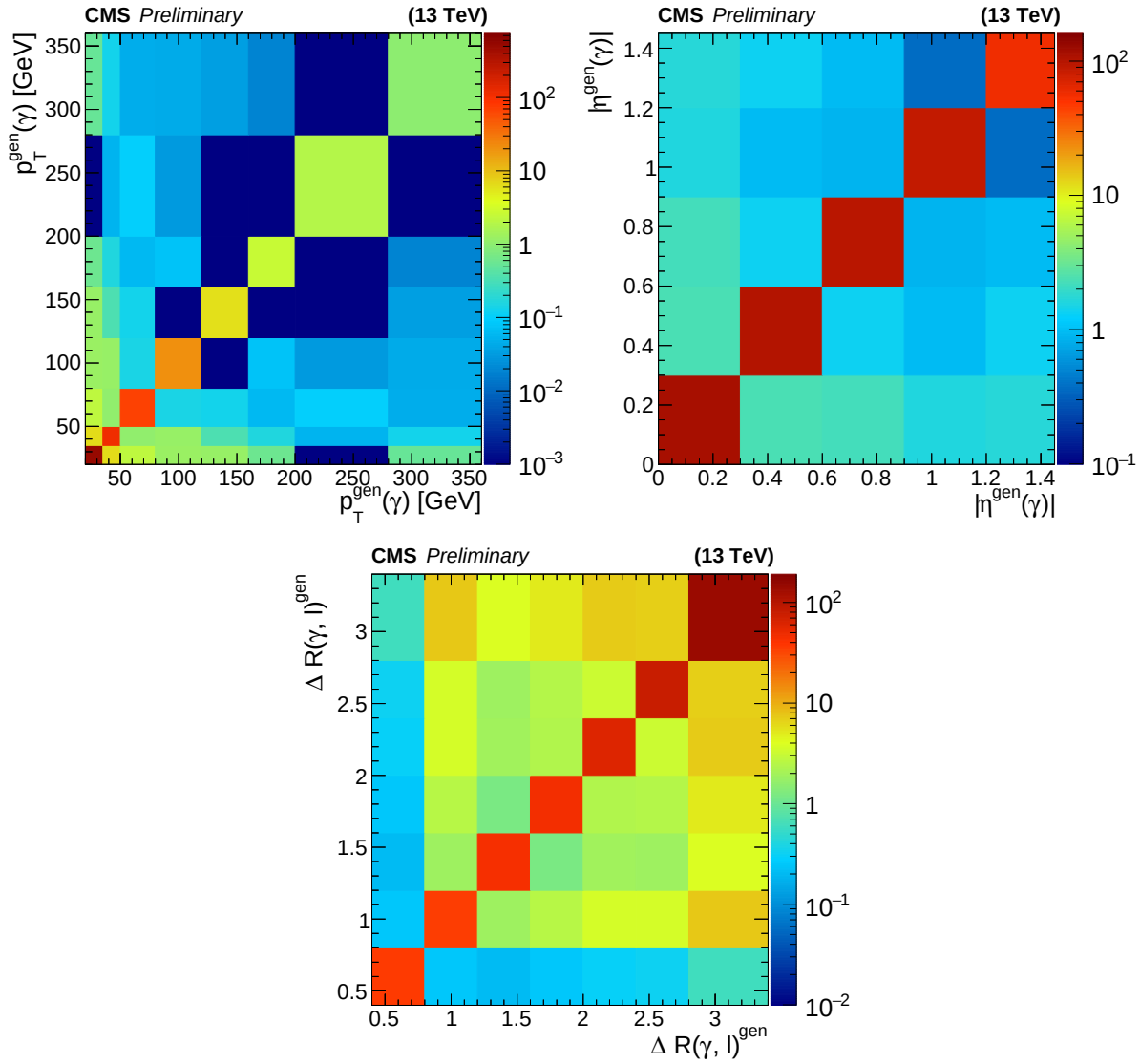

Figure 10: The covariance matrices of the unfolded differential measurement for $p_T(\gamma)$ (left), $|\eta(\gamma)|$ (right), and $\Delta R(\ell, \gamma)$ (bottom).

8 Effective field theory interpretation

Owing to the special role of the SM top quark, many BSM models predict anomalous couplings of the top quark to the electroweak gauge bosons [72–78]. The differential cross section measurement is interpreted in SMEFT in the Warsaw basis [8], formed by 59 independent Wilson coefficients of mass dimension 6. Among them, 15 are important for top quark interactions [79], which in general have a large impact on processes other than $\mathrm{t\bar{t}}\gamma$. The intimate relation between the Z boson and the photon in the electroweak symmetry breaking (EWSB) of the SM gauge symmetry, equip the $\mathrm{t\bar{t}Z}$ and the $\mathrm{t\bar{t}}\gamma$ final states with complementary constraining power [80, 81] for the operators c_{tZ} and c_{tZ}^{I}. The $\mathrm{t}\gamma$ anomalous vertex however is more sensitive to c_{tZ} than the tZ vertex [9] and in combination with the larger production cross section of the $\mathrm{t\bar{t}}\gamma$ process, the SM gauge symmetry thus makes measurements in $\mathrm{t\bar{t}}\gamma$ final states very competitive. The operators c_{tZ} and c_{tZ}^{I} induce electroweak dipole moments of the top quarks and the spectrum of $p_T(\gamma)$ is a sensitive probe to such modifications, while other observables, e.g. $|\eta(\gamma)|$ or $\Delta R(\ell, \gamma)$, are found to be insensitive.

The SR3 and SR4p signal regions are kept separate and the $p_T(\gamma)$ thresholds from Fig. 8 (left) are used to construct a binned likelihood function $L(\theta)$ as a product of Poisson probabilities from the yields in the signal and control regions. The nuisance parameters are labeled by θ and the profile likelihood ratio $q = -2\ln(L(\hat{\theta}, \vec{C})/L(\hat{\theta}_{\mathrm{max}}))$ is the test statistic. Here, $\hat{\theta}$ is the set of nuisance parameters maximizing the likelihood function at a BSM point defined by the Wilson coefficients collectively denoted by $\vec{C}$. In the denominator, $\hat{\theta}_{\mathrm{max}}$ maximizes the likelihood function for all model parameters under consideration.

Figure 11 (bottom) shows the best-fit result in the two-dimensional plane spanned by c_{tZ} and c_{tZ}^{I} and the log-likelihood scan. Models with nonzero electroweak dipole moments predict a harder $p_T(\gamma)$ spectrum that is not observed in data. The SM prediction is within the 95% confidence interval of the best-fit value of the c_{tZ} and c_{tZ}^{I} coefficients.

Figure 11 (top left, right) displays the one-dimensional scans, where in each figure, the other Wilson coefficient is set to zero. The corresponding 1D confidence intervals at 68 and 95% CL are listed in Table 6 and are the most stringent direct constraints to date.

Data set	Wilson coefficient	68% CL interval	95% CL interval
expected	c_{tZ}	[-0.19, 0.21]	[-0.29, 0.32]
	c_{tZ}^{I}	[-0.20, 0.20]	[-0.30, 0.31]
observed	c_{tZ}	[-0.35, -0.16]	[-0.42, 0.38]
	c_{tZ}^{I}	[-0.35, -0.16], [0.17, 0.35]	[-0.42, 0.42]

Table 6: Summary of the 1D confidence intervals at 68 and 95% CL.

9 Summary

A measurement of top quark pair production in association with a photon using a data sample of proton-proton collisions at $\sqrt{s} = 13\,\mathrm{TeV}$, corresponding to an integrated luminosity of 137 fb^{-1}, collected with the CMS detector at the LHC has been presented. The analysis was performed in the three- and at least four-jet final states. A data driven approach is used to estimate the background in the signal regions. The measured inclusive cross section is $\sigma^{\mathrm{fid.}}(\mathrm{t\bar{t}}\gamma) = 800 \pm 46\,(\mathrm{syst}) \pm 7\,(\mathrm{stat})\,\mathrm{fb}$ and is in good agreement with the standard model prediction.

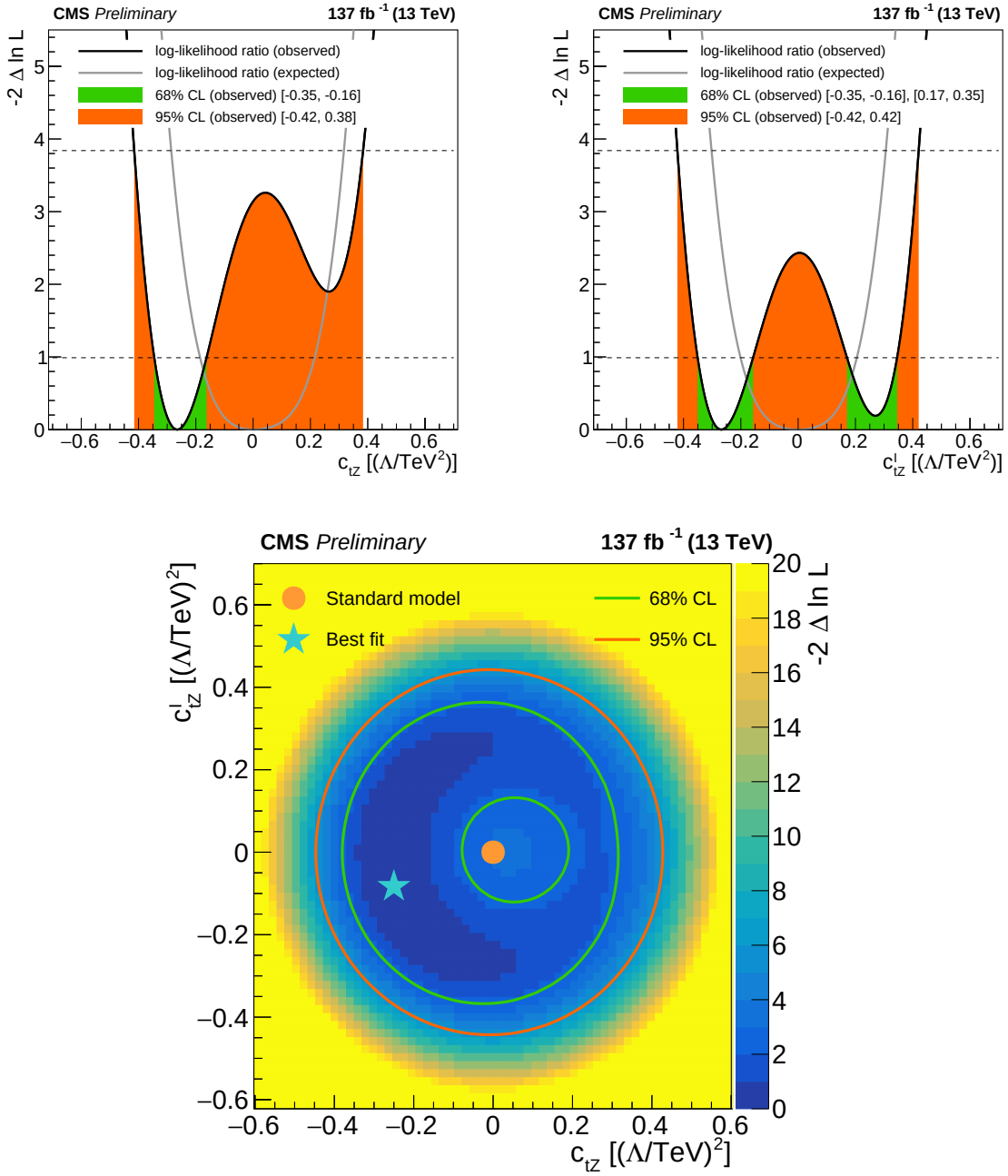

Figure 11: Results of one-dimensional scans for the Wilson coefficients c_{tZ} (left) and c^{I}_{tZ} (right), and for the two-dimensional plane (bottom). The shading quantified by the color scale on the right reflects the negative log-likelihood ratio with respect to the best-fit value that is designated by the star. The green and orange lines indicate the 68 and 95% CL contours from the fit, respectively. The allowed areas are those between the two green contours and that inside the orange contour. The dot shows the SM prediction.

Absolute and normalized differential cross sections for the transverse momentum of the $p_T(\gamma)$, $|\eta(\gamma)|$, and $\Delta R(\ell, \gamma)$ are measured. The measurement is also interpreted in terms of Wilson coefficients in the context of SMEFT. The confidence intervals for the Wilson coefficients c_{tZ} and c_{tZ}^I are the strongest to date.

References

[1] O. Bessidskaia Bylund et al., "Probing top quark neutral couplings in the standard model effective field theory at NLO in QCD", *JHEP* **05** (2016) 052, doi:10.1007/JHEP05(2016)052, arXiv:1601.08193.

[2] CDF Collaboration, "Evidence for $t\bar{t}\gamma$ production and measurement of $\sigma_{t\bar{t}\gamma}/\sigma_{t\bar{t}}$", *Phys. Rev. D* **48** (2011) 031104, doi:10.1103/PhysRevD.84.031104, arXiv:1106.3970.

[3] ATLAS Collaboration, "Observation of top-quark pair production in association with a photon and measurement of the $t\bar{t}\gamma$ production cross section in pp collisions at $\sqrt{s} = 7$ TeV using the ATLAS detector", *Phys. Rev. D* **91** (2015) 072007, doi:10.1103/PhysRevD.91.072007, arXiv:1502.00586.

[4] ATLAS Collaboration, "Measurement of the $t\bar{t}\gamma$ production cross section in proton-proton collisions at $\sqrt{s} = 8$ TeV with the ATLAS detector", *JHEP* **11** (2017) 086, doi:10.1007/JHEP11(2017)086, arXiv:1706.03046.

[5] CMS Collaboration, "Measurement of the semileptonic $t\bar{t} + \gamma$ production cross section in pp collisions at $\sqrt{s} = 8$ TeV", *JHEP* **10** (2017) 006, doi:10.1007/JHEP10(2017)006, arXiv:1706.08128.

[6] ATLAS Collaboration, "Measurements of inclusive and differential fiducial cross-sections of $t\bar{t}\gamma$ production in leptonic final states at $\sqrt{s} = 13$ TeV in ATLAS", *Eur. Phys. J. C* **79** (2019) 382, doi:10.1140/epjc/s10052-019-6849-6, arXiv:1812.01697.

[7] ATLAS Collaboration, "Measurements of inclusive and differential cross-sections of combined $t\bar{t}\gamma$ and $tW\gamma$ production in the $e\mu$ channel at 13 TeV with the ATLAS detector", *JHEP* **09** (2020) 049, doi:10.1007/JHEP09(2020)049, arXiv:2007.06946.

[8] B. Grzadkowski, M. Iskrzynski, M. Misiak, and J. Rosiek, "Dimension-six terms in the standard model Lagrangian", *JHEP* **10** (2010) 085, doi:10.1007/JHEP10(2010)085, arXiv:1008.4884.

[9] D. Barducci et al., "Interpreting top-quark LHC measurements in the standard-model effective field theory", (2, 2018). arXiv:1802.07237.

[10] J. Alwall et al., "The automated computation of tree-level and next-to-leading order differential cross sections, and their matching to parton shower simulations", *JHEP* **07** (2014) 079, doi:10.1007/JHEP07(2014)079, arXiv:1405.0301.

[11] P. Nason, "A new method for combining NLO QCD with shower Monte Carlo algorithms", *JHEP* **11** (2004) 040, doi:10.1088/1126-6708/2004/11/040, arXiv:hep-ph/0409146.

[12] S. Frixione, P. Nason, and C. Oleari, "Matching NLO QCD computations with Parton Shower simulations: the POWHEG method", *JHEP* **11** (2007) 070, doi:10.1088/1126-6708/2007/11/070, arXiv:0709.2092.

[13] S. Alioli, P. Nason, C. Oleari, and E. Re, "A general framework for implementing NLO calculations in shower Monte Carlo programs: the POWHEG BOX", *JHEP* **06** (2010) 043, doi:10.1007/JHEP06(2010)043, arXiv:1002.2581.

[14] J. M. Campbell, R. K. Ellis, P. Nason, and E. Re, "Top-pair production and decay at NLO matched with parton showers", *JHEP* **04** (2015) 114, doi:10.1007/JHEP04(2015)114, arXiv:1412.1828.

[15] S. Alioli, P. Nason, C. Oleari, and E. Re, "NLO single-top production matched with shower in POWHEG: s- and t-channel contributions", *JHEP* **09** (2009) 111, doi:10.1088/1126-6708/2009/09/111, arXiv:0907.4076. [Erratum: doi:10.1007/JHEP02(2010)011].

[16] S. Frixione, P. Nason, and G. Ridolfi, "A positive-weight next-to-leading-order Monte Carlo for heavy flavour hadroproduction", *JHEP* **09** (2007) 126, doi:10.1088/1126-6708/2007/09/126, arXiv:0707.3088.

[17] M. Czakon and A. Mitov, "Top++: A Program for the Calculation of the Top-Pair Cross-Section at Hadron Colliders", *Comput. Phys. Commun.* **185** (2014) 2930, doi:10.1016/j.cpc.2014.06.021, arXiv:1112.5675.

[18] S. Dulat et al., "New parton distribution functions from a global analysis of quantum chromodynamics", *Phys. Rev. D* **93** (2016) 033006, doi:10.1103/PhysRevD.93.033006, arXiv:1506.07443.

[19] M. Aliev et al., "HATHOR: HAdronic Top and Heavy quarks crOss section calculatoR", *Comput. Phys. Commun.* **182** (2011) 1034, doi:10.1016/j.cpc.2010.12.040, arXiv:1007.1327.

[20] P. Kant et al., "HATHOR for single top-quark production: Updated predictions and uncertainty estimates for single top-quark production in hadronic collisions", *Comput. Phys. Commun.* **191** (2015) 74, doi:10.1016/j.cpc.2015.02.001, arXiv:1406.4403.

[21] N. Kidonakis, "Theoretical results for electroweak-boson and single-top production", *PoS* **DIS2015** (2015) 170, doi:10.22323/1.247.0170, arXiv:1506.04072.

[22] K. Melnikov and F. Petriello, "Electroweak gauge boson production at hadron colliders through $O(\alpha_S^2)$", *Phys. Rev. D* **74** (2006) 114017, doi:10.1103/PhysRevD.74.114017, arXiv:hep-ph/0609070.

[23] S. Catani et al., "Vector boson production at hadron colliders: a fully exclusive QCD calculation at NNLO", *Phys. Rev. Lett.* **103** (2009) 082001, doi:10.1103/PhysRevLett.103.082001, arXiv:0903.2120.

[24] C. Anastasiou, L. J. Dixon, K. Melnikov, and F. Petriello, "High precision QCD at hadron colliders: Electroweak gauge boson rapidity distributions at NNLO", *Phys. Rev. D* **69** (2004) 094008, doi:10.1103/PhysRevD.69.094008, arXiv:hep-ph/0312266.

[25] S. Dittmaier, A. Huss, and C. Schwinn, "Mixed QCD-electroweak $O(\alpha_S\alpha)$ corrections to Drell-Yan processes in the resonance region: pole approximation and non-factorizable corrections", *Nucl. Phys. B* **885** (2014) 318, doi:10.1016/j.nuclphysb.2014.05.027, arXiv:1403.3216.

[26] J. M. Lindert et al., "Precise predictions for $V+$ jets dark matter backgrounds", *Eur. Phys. J. C* **77** (2017) 829, doi:10.1140/epjc/s10052-017-5389-1, arXiv:1705.04664.

[27] M. V. Garzelli, A. Kardos, C. G. Papadopoulos, and Z. Trocsanyi, "$t\bar{t}W^{\pm}$ and $t\bar{t}Z$ hadroproduction at NLO accuracy in QCD with parton shower and hadronization effects", *JHEP* **11** (2012) 056, doi:10.1007/JHEP11(2012)056, arXiv:1208.2665.

[28] S. Frixione et al., "Electroweak and QCD corrections to top-pair hadroproduction in association with heavy bosons", *JHEP* **06** (2015) 184, doi:10.1007/JHEP06(2015)184, arXiv:1504.03446.

[29] M. Beneke, P. Falgari, S. Klein, and C. Schwinn, "Hadronic top-quark pair production with NNLL threshold resummation", *Nucl. Phys. B* **855** (2012) 695, doi:10.1016/j.nuclphysb.2011.10.021, arXiv:1109.1536.

[30] M. Cacciari et al., "Top-pair production at hadron colliders with next-to-next-to-leading logarithmic soft-gluon resummation", *Phys. Lett. B* **710** (2012) 612, doi:10.1016/j.physletb.2012.03.013, arXiv:1111.5869.

[31] P. Bärnreuther, M. Czakon, and A. Mitov, "Percent Level Precision Physics at the Tevatron: First Genuine NNLO QCD Corrections to $q\bar{q} \to t\bar{t} + X$", *Phys. Rev. Lett.* **109** (2012) 132001, doi:10.1103/PhysRevLett.109.132001, arXiv:1204.5201.

[32] M. Czakon and A. Mitov, "NNLO corrections to top-pair production at hadron colliders: the all-fermionic scattering channels", *JHEP* **12** (2012) 054, doi:10.1007/JHEP12(2012)054, arXiv:1207.0236.

[33] M. Czakon and A. Mitov, "NNLO corrections to top pair production at hadron colliders: the quark-gluon reaction", *JHEP* **01** (2013) 080, doi:10.1007/JHEP01(2013)080, arXiv:1210.6832.

[34] M. Czakon, P. Fiedler, and A. Mitov, "Total Top-Quark Pair-Production Cross Section at Hadron Colliders Through $O(\alpha_S^4)$", *Phys. Rev. Lett.* **110** (2013) 252004, doi:10.1103/PhysRevLett.110.252004, arXiv:1303.6254.

[35] T. Gehrmann et al., "W^+W^- Production at Hadron Colliders in Next to Next to Leading Order QCD", *Phys. Rev. Lett.* **113** (2014) 212001, doi:10.1103/PhysRevLett.113.212001, arXiv:1408.5243.

[36] T. Sjöstrand et al., "An introduction to PYTHIA 8.2", *Comput. Phys. Commun.* **191** (2015) 159, doi:10.1016/j.cpc.2015.01.024, arXiv:1410.3012.

[37] P. Skands, S. Carrazza, and J. Rojo, "Tuning PYTHIA 8.1: the Monash 2013 tune", *Eur. Phys. J. C* **74** (2014) 3024, doi:10.1140/epjc/s10052-014-3024-y, arXiv:1404.5630.

[38] CMS Collaboration, "Event generator tunes obtained from underlying event and multiparton scattering measurements", *Eur. Phys. J. C* **76** (2016) 155, doi:10.1140/epjc/s10052-016-3988-x, arXiv:1512.00815.

[39] CMS Collaboration, "Extraction and validation of a new set of CMS PYTHIA8 tunes from underlying-event measurements", *Eur. Phys. J. C* **80** (2020) 4, doi:10.1140/epjc/s10052-019-7499-4, arXiv:1903.12179.

[40] NNPDF Collaboration, "Parton distributions for the LHC Run II", *JHEP* **04** (2015) 040, doi:10.1007/JHEP04(2015)040, arXiv:1410.8849.

[41] NNPDF Collaboration, "Parton distributions from high-precision collider data", *Eur. Phys. J. C* **77** (2017) 663, doi:10.1140/epjc/s10052-017-5199-5, arXiv:1706.00428.

[42] J. Alwall et al., "Comparative study of various algorithms for the merging of parton showers and matrix elements in hadronic collisions", *Eur. Phys. J. C* **53** (2008) 473, doi:10.1140/epjc/s10052-007-0490-5, arXiv:0706.2569.

[43] R. Frederix and S. Frixione, "Merging meets matching in MC@NLO", *JHEP* **12** (2012) 061, doi:10.1007/JHEP12(2012)061, arXiv:1209.6215.

[44] GEANT4 Collaboration, "GEANT4—a simulation toolkit", *Nucl. Instrum. Meth. A* **506** (2003) 250, doi:10.1016/S0168-9002(03)01368-8.

[45] CMS Collaboration, "Measurement of the inelastic proton-proton cross section at $\sqrt{s} = 13$ TeV", *JHEP* **07** (2018) 161, doi:10.1007/JHEP07(2018)161, arXiv:1802.02613.

[46] CMS Collaboration, "Particle-flow reconstruction and global event description with the CMS detector", *JINST* **12** (2017) P10003, doi:10.1088/1748-0221/12/10/P10003, arXiv:1706.04965.

[47] CMS Collaboration, "Performance of electron reconstruction and selection with the CMS detector in proton-proton collisions at $\sqrt{s} = 8$ TeV", *JINST* **10** (2015) P06005, doi:10.1088/1748-0221/10/06/P06005, arXiv:1502.02701.

[48] CMS Collaboration, "Performance of Photon Reconstruction and Identification with the CMS Detector in Proton-Proton Collisions at sqrt(s) = 8 TeV", *JINST* **10** (2015) P08010, doi:10.1088/1748-0221/10/08/P08010, arXiv:1502.02702.

[49] M. Cacciari, G. P. Salam, and G. Soyez, "The anti-k_t jet clustering algorithm", *JHEP* **04** (2008) 063, doi:10.1088/1126-6708/2008/04/063, arXiv:0802.1189.

[50] M. Cacciari, G. P. Salam, and G. Soyez, "FastJet User Manual", *Eur. Phys. J. C* **72** (2012) 1896, doi:10.1140/epjc/s10052-012-1896-2, arXiv:1111.6097.

[51] CMS Collaboration, "Electron and photon reconstruction and identification with the CMS experiment at the CERN LHC", *submitted to JINST* (2020) arXiv:2012.06888.

[52] CMS Collaboration, "Jet energy scale and resolution in the CMS experiment in pp collisions at 8 TeV", *JINST* **12** (2017) P02014, doi:10.1088/1748-0221/12/02/P02014, arXiv:1607.03663.

[53] CMS Collaboration, "Identification of heavy-flavour jets with the CMS detector in pp collisions at 13 TeV", *JINST* **13** (2018) P05011, doi:10.1088/1748-0221/13/05/P05011, arXiv:1712.07158.

[54] M. Cacciari, G. P. Salam, and G. Soyez, "The Catchment Area of Jets", *JHEP* **04** (2008) 005, doi:10.1088/1126-6708/2008/04/005, arXiv:0802.1188.

[55] CMS Collaboration, "CMS luminosity measurement for the 2016 data taking period", CMS Physics Analysis Summary CMS-PAS-LUM-17-001, 2017.

[56] CMS Collaboration, "CMS luminosity measurement for the 2017 data taking period", CMS Physics Analysis Summary CMS-PAS-LUM-17-004, 2017.

[57] CMS Collaboration, "CMS luminosity measurement for the 2018 data-taking period at $\sqrt{s} = 13$ TeV", CMS Physics Analysis Summary CMS-PAS-LUM-18-002, 2019.

[58] ATLAS Collaboration, "Measurement of the Inelastic Proton-Proton Cross Section at $\sqrt{s} = 13$ TeV with the ATLAS Detector at the LHC", *Phys. Rev. Lett.* **117** (2016) 182002, doi:10.1103/PhysRevLett.117.182002, arXiv:1606.02625.

[59] CMS Collaboration, "Performance of CMS muon reconstruction in pp collision events at $\sqrt{s} = 7$ TeV", *JINST* **7** (2012) P10002, doi:10.1088/1748-0221/7/10/P10002, arXiv:1206.4071.

[60] CMS Collaboration, "Energy Calibration and Resolution of the CMS Electromagnetic Calorimeter in pp Collisions at $\sqrt{s} = 7$ TeV", *JINST* **8** (2013) P09009, doi:10.1088/1748-0221/8/09/P09009, arXiv:1306.2016.

[61] CMS Collaboration, "Identification of b-quark jets with the CMS experiment", *JINST* **8** (2013) P04013, doi:10.1088/1748-0221/8/04/P04013, arXiv:1211.4462.

[62] J. Butterworth et al., "PDF4LHC recommendations for LHC Run II", *J. Phys. G* **43** (2016) 023001, doi:10.1088/0954-3899/43/2/023001, arXiv:1510.03865.

[63] R. D. Ball et al., "Parton distributions with LHC data", *Nucl. Phys. B* **867** (2013) 244, doi:10.1016/j.nuclphysb.2012.10.003, arXiv:1207.1303.

[64] A. D. Martin, W. J. Stirling, R. S. Thorne, and G. Watt, "Uncertainties on α_S in global PDF analyses and implications for predicted hadronic cross sections", *Eur. Phys. J. C* **64** (2009) 653, doi:10.1140/epjc/s10052-009-1164-2, arXiv:0905.3531.

[65] J. Gao et al., "CT10 next-to-next-to-leading order global analysis of QCD", *Phys. Rev. D* **89** (2014) 033009, doi:10.1103/PhysRevD.89.033009, arXiv:1302.6246.

[66] S. Argyropoulos and T. Sjöstrand, "Effects of color reconnection on $t\bar{t}$ final states at the LHC", *JHEP* **11** (2014) 043, doi:10.1007/JHEP11(2014)043, arXiv:1407.6653.

[67] J. R. Christiansen and P. Z. Skands, "String formation beyond leading colour", *JHEP* **08** (2015) 003, doi:10.1007/JHEP08(2015)003, arXiv:1505.01681.

[68] The ATLAS Collaboration, The CMS Collaboration, The LHC Higgs Combination Group Collaboration, "Procedure for the LHC Higgs boson search combination in Summer 2011", Technical Report CMS-NOTE-2011-005. ATL-PHYS-PUB-2011-11, CERN, Geneva, Aug, 2011.

[69] G. Cowan, K. Cranmer, E. Gross, and O. Vitells, "Asymptotic formulae for likelihood-based tests of new physics", *Eur. Phys. J. C* **71** (2011) 1554, doi:10.1140/epjc/s10052-011-1554-0, arXiv:1007.1727. [Erratum: doi:10.1140/epjc/s10052-013-2501-z].

[70] G. Cowan, "Statistical data analysis". Clarendon Press, Oxford, 1998.

[71] S. Schmitt, "TUnfold, an algorithm for correcting migration effects in high energy physics", *JINST* **7** (2012) T10003, doi:10.1088/1748-0221/7/10/T10003, arXiv:1205.6201.

[72] W. Hollik et al., "Top dipole form-factors and loop induced CP violation in supersymmetry", *Nucl. Phys. B* **551** (1999) 3, doi:10.1016/S0550-3213(99)00201-1, arXiv:hep-ph/9812298. [Erratum: doi:10.1016/S0550-3213(99)00396-X].

[73] K. Agashe, G. Perez, and A. Soni, "Collider Signals of Top Quark Flavor Violation from a Warped Extra Dimension", *Phys. Rev. D* **75** (2007) 015002, doi:10.1103/PhysRevD.75.015002, arXiv:hep-ph/0606293.

[74] A. L. Kagan, G. Perez, T. Volansky, and J. Zupan, "General Minimal Flavor Violation", *Phys. Rev. D* **80** (2009) 076002, doi:10.1103/PhysRevD.80.076002, arXiv:0903.1794.

[75] T. Ibrahim and P. Nath, "The Top quark electric dipole moment in an MSSM extension with vector like multiplets", *Phys. Rev. D* **82** (2010) 055001, doi:10.1103/PhysRevD.82.055001, arXiv:1007.0432.

[76] T. Ibrahim and P. Nath, "The Chromoelectric Dipole Moment of the Top Quark in Models with Vector Like Multiplets", *Phys. Rev. D* **84** (2011) 015003, doi:10.1103/PhysRevD.84.015003, arXiv:1104.3851.

[77] C. Grojean, O. Matsedonskyi, and G. Panico, "Light top partners and precision physics", *JHEP* **10** (2013) 160, doi:10.1007/JHEP10(2013)160, arXiv:1306.4655.

[78] F. Richard, "Can LHC observe an anomaly in ttZ production?", (2013). arXiv:1304.3594.

[79] C. Zhang and S. Willenbrock, "Effective-field-theory approach to top-quark production and decay", *Phys. Rev. D* **83** (2011) 034006, doi:10.1103/PhysRevD.83.034006, arXiv:1008.3869.

[80] Röntsch, Raoul and Schulze, Markus, "Probing top-Z dipole moments at the LHC and ILC", *JHEP* **08** (2015) 044, doi:10.1007/JHEP08(2015)044, arXiv:1501.05939.

[81] M. Schulze and Y. Soreq, "Pinning down electroweak dipole operators of the top quark", *Eur. Phys. J. C* **76** (2016) 466, doi:10.1140/epjc/s10052-016-4263-x, arXiv:1603.08911.